Soft Matter

Instabilities and patterns in a submerged jelling jet

Journal:	*Soft Matter*
Manuscript ID	SM-ART-04-2021-000517.R1
Article Type:	Paper
Date Submitted by the Author:	26-Aug-2021
Complete List of Authors:	Chakrabarti, Aditi; Harvard University, School of Engineering and Applied Science Al-Mosleh, Salem; Harvard University, School of Engineering and Applied Science Mahadevan, L.; Harvard University Faculty of Arts and Sciences, School of Engineering and Applied Science; Harvard University,

Soft Matter

ARTICLE TYPE

Cite this: DOI: 00.0000/xxxxxxxxxx

Instabilities and patterns in a submerged jelling jet†

Aditi Chakrabarti,[a‡] Salem Al-Mosleh,[a‡] and L. Mahadevan[abc*]

Received Date
Accepted Date

DOI: 00.0000/xxxxxxxxxx

When a thin stream of aqueous sodium alginate is extruded into a reacting calcium chloride bath, it polymerizes into a soft elastic tube that spontaneously forms helical coils due to the ambient fluid drag. We quantify the onset of this drag-induced instability and its nonlinear evolution using experiments, and explain the results using a combination of scaling, theory and simulations. By co-extruding a second (internal) liquid within the aqueous sodium alginate jet and varying the the diameter of the jet and the rates of co-extrusion of the two liquids, we show that we can tune the local composition of the composite filament and the nature of the ensuing instabilities to create soft filaments of variable relative buoyancy, shape and mechanical properties. All together, by harnessing the fundamental varicose (jetting) and sinuous (buckling) instabilities associated with the extrusion of a submerged jelling filament, we show that it is possible to print complex three-dimensional filamentous structures in an ambient fluid.

Slender filamentous structures buckle, fold and coil on a range of length scales spanning the nanometric to the macrometric. For example, an elastic rope fed uniformly toward a horizontal plane coils into a spool[1–3]; similar behavior is seen with a slender jet of viscous fluid[4–7]. In both cases, the presence of the plane boundary leads to compressive stresses, while geometric scale separation implies the dominance of bending deformations. Quantitative predictions for the coiling rates and radii then arise from the balance of internal elastic or viscous forces and inertia and/or gravity. The patterns arising from these instabilities have also been harnessed to fabricate structures by coupling them to phase changes in solidifying polymers and glass[8–10]. Here, partly inspired by these examples, and partly by the quest to pattern filaments in three dimensions without a sacrificial scaffold as exemplified by the 3Doodler pen[11], we ask if there are instabilities and patterns that can be harnessed when a filament moves through an ambient fluid while also changing from a liquid to solid. This is seen in high speed liquid polymer extrusion in air[12], where solvent-loss driven solidification happens so fast that it is almost impossible to control the instability. But could one extrude a viscous filament in an aqueous bath containing a crosslinker that causes the stream to polymerize, buckle and coil due to the resisting viscous drag forces from the surrounding medium, even in the absence of compressive stresses due to a solid boundary? And then control the patterns by varying the extrusion rate and even the properties by co-extruding a second fluid within the jelling jet?

We answer both questions in the affirmative. By extruding an alginate solution into a calcium bath, we study the onset of a periodic coiling instability as well as its saturation via a combination of scaling analysis, stability theory and computation. By introducing a second fluid at the inlet, we show that we can add periodic droplet inclusions of oil and gas to the soft filaments. This allows for a single-step fabrication protocol to make a continuous soft filament of varying composition, stiffness, curvature and buoyancy that can be used to write and draw patterns in 3 dimensions in an ambient fluid without a sacrificial substrate.

Experimental observations

Our experimental setup (Fig. 1A) for the fabrication of single phase gel filaments and tubes uses a 2% w/w sodium alginate solution, dyed with 0.01% w/w methylene blue, filled in plastic syringes, and dispensed inside an aqueous bath (viscosity μ) of calcium chloride salt (150mM in water) at extrusion rates (Q_o, 0.1 - 20 ml/min) via needles (inner diameter d, 0.1-2mm) (See Appendix A.1 and Movie S1 for more details). For all the experiments, the concentrations of sodium alginate and calcium chloride in the respective aqueous solutions were kept fixed, thereby fixing the reaction rate (k) of gelation. As the polymerization progresses[13], the elastic Young's modulus of the crosslinked alginate tubes increases from hundreds of pascals (within a few seconds) to tens of kilopascals (over several minutes). We quantify this change in the stiffness via simple gravity-driven bending of

[a] John A. Paulson School of Engineering and Applied Sciences, Harvard University, Cambridge, MA 02138, USA.
[b] Department of Physics, Harvard University, Cambridge, MA 02138, USA.
[c] Department of Organismic and Evolutionary Biology, Harvard University, Cambridge, MA 02138, USA.
‡ These authors contributed equally to this work.
* To whom correspondence should be addressed. E-mail: lmahadev@g.harvard.edu.
† Electronic Supplementary Information (ESI) available: [details of any supplementary information available should be included here]. See DOI: 10.1039/cXsm00000x/

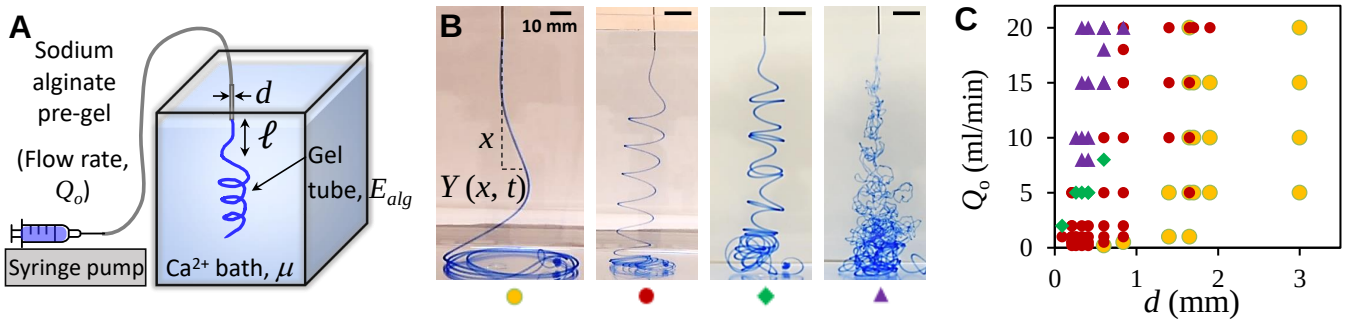

Fig. 1 Instability of a submerged jelling jet. (A) Schematic of the experimental setup that is used to obtain the drag induced coiling instability of a solidifying sodium alginate gel tube in a water bath containing 150 mM calcium chloride. A syringe pump is used to deliver the 2% sodium alginate solution, dyed with methylene blue, at a prescribed flow rate (Q_o) via a blunt-tipped needle (inner diameter, d) into the calcium bath. As the sodium alginate solution contacts the calcium ions in the water bath, it begins to crosslink to form an elastic soft tube and then buckles due to the compression induced by the viscous drag of the surrounding liquid. (B) As the flow rate Q_o is increased, we get a transition of behaviors from classical rope coiling (yellow circles, 18G needle, $d = 0.84$mm at Q_o=0.5ml/min), to drag-induced elastic coiling (red circles, 22G needle, $d = 0.41$mm at Q_o=0.5ml/min), period doubling (green diamonds, 22G needle, $d = 0.41$mm at Q_o=5ml/min) to chaotic crumpling (purple triangles, 22G needle, $d = 0.41$mm at Q_o=20ml/min) (See Movie S2). All scale bars are 10 mm. (C) Phase space of the instability regimes shown in (B) plotted as a function of the flow rates of the alginate extrudate Q_o and the needle inner diameters d used.

filament segments, removed at different times from the calcium chloride solution (Appendix A.2, Fig. A3 A-B).

For extrusion from a given needle diameter (d) at very low flow rates (Q_o), a thin stream of alginate extruding inside the calcium bath polymerizes to form an elastic tube. In this regime, when the elastic tube pushes against the base of the container, it starts to coil like an elastic rope[1,2](Fig. 1B, first panel), due to the resulting compressive stresses induced in the filament. However, as Q_o is increased, the polymerized elastic tube begins to buckle over a characteristic length ℓ much smaller than the falling height, and spontaneously forms loosely coiled helices (radius, R, and vertical spacing between coils, Λ) as it falls through the liquid bath (Fig. 1B, second panel and Appendix, Fig.A1). In this regime, there is no influence of the floor. Further increase in the extrusion rate Q_o leads to more complex patterns that exhibit signs of period doubling in the spacing between the helical coils(Fig. 1B, third panel), and when Q_o is very large, the jet polymerizes and crumples chaotically forming rough tubes that stay within a conical region (Fig. 1B, last panel, Appendix, Movies S2-S3). The phase space of patterns and morphologies is determined by the extrusion rate (Q_o) and the needle diameter (d) as shown in Fig. 1C (Movie S2).

Scaling analysis and stability theory

To understand these patterns, we note that if the polymerization process with a rate k is relatively fast, i.e. $kd/v \gg 1$ (v is the speed of extrusion and d the diameter of the needle which is comparable to the diameter of the tube ($2r$) that forms), the polymerized filament behaves like an elastic filament of bending stiffness B. If the filament buckles over a characteristic scale ℓ, we can balance the resisting bending torque B/ℓ in the filament with the forcing viscous torque from the ambient fluid that scales as $\mu v \ell^2$ to find a characteristic length scale[14,15]

$$\ell \sim \left(\frac{B}{\mu\, v}\right)^{1/3}, \tag{1}$$

above which the extrudate should buckle and coil into a helix spontaneously. Beyond the onset of buckling, we expect the radius of the helical coil to follow this same scaling with $R \sim \ell$, while the frequency of coiling is expected to behave as

$$\omega \sim v/\ell \sim v^{4/3} \left(\frac{\mu}{B}\right)^{1/3}. \tag{2}$$

Plotting the experimental data for buckling length ℓ, coiling radius R and coiling frequency ω (Fig. 2), we find that the data agree well with the scaling expressions obtained above. The vertical spacing between the coils (Λ) also remain steady while the stack of freshly coiled alginate tubes descends through the ambient calcium solution (Fig. A1 and Movie S1). Furthermore, we see that the entire range of scenarios from gravity-induced to drag-induced elastic coiling can be collapsed to a single universal scaling law that interpolates between two limits, gravity-induced coiling and drag-induced coiling, leading to an expression

$$\ell \sim (B/(\mu v + \Delta\rho g r^2))^{1/3} \tag{3}$$

where $\Delta\rho$ is the density difference between the alginate tubes and the surrounding calcium bath (Fig. 3). In the limit of no external fluid, we recover the well-known scaling law for elastic folding and coiling[1,16] $\ell_g \sim (B/\rho g r^2)^{1/3}$.

Moving beyond a scaling analysis, we consider the linear stability of a thin elastic rod with length L, moving in a fluid with viscosity μ at a speed v, in the limit of low Reynolds number, i.e. $\rho v L/\mu \ll 1$. For a flexible rod whose center line follows a path $Y(x,t)$ (see Fig. 1B) that is only slightly deviated from being straight, force balance in the tangential and normal directions yields

$$0 = v\,\mu_s + \partial_x T(x,t), \tag{4}$$

$$0 = 2\,\mu_s\,\partial_t Y(x,t) + v\,\mu_s\,\partial_x Y(x,t) + B\,\partial_x^4 Y(x,t) - \partial_x\left(T(x,t)\,\partial_x Y(x,t)\right). \tag{5}$$

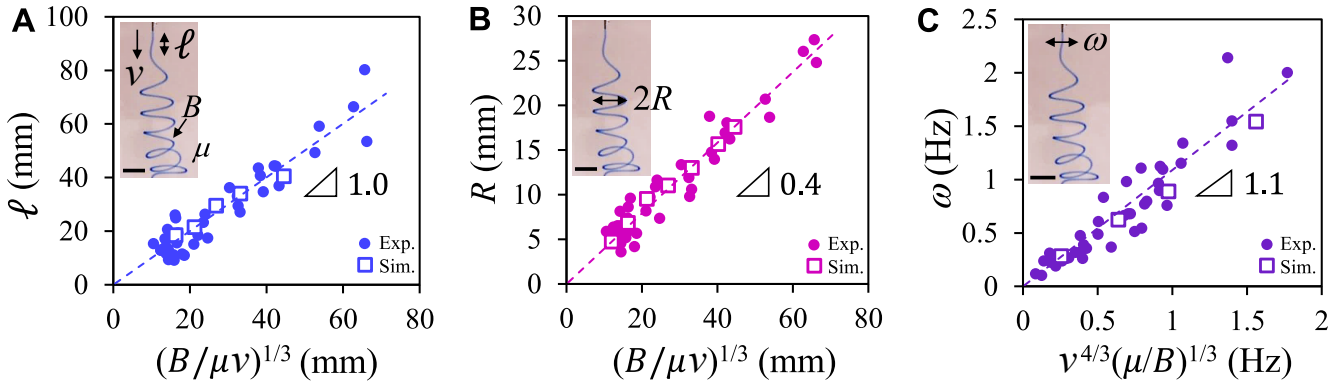

Fig. 2 Understanding the instability. (A) The directly measured buckling length ℓ is plotted as a function of $(B/\mu v)^{1/3}$ across various experiments (closed circles), where needle diameters d varied from 0.1 mm to 2 mm, and flow rates varied from 0.2 ml/min to 20 ml/min. Simulation data are shown with open square symbols. (Inset) Experimental snapshot to define ℓ, extrusion velocity v, viscosity of bath μ and bending stiffness B of the polymerized filament. (B) Characterization of the drag induced elastic coiling instability via coiling radius (R) plotted as a function of the scaling relationship $(B/\mu v)^{1/3}$, with a slope of 0.4 for the linear regression for both experiments and simulation. (Inset) Definite of coiling radius R. (C) The frequency of coiling ω for the experimental and simulation data shows that it scales as $v^{4/3}(\mu/B)^{1/3}$ with a slope of 1.1. (Inset) Definition of ω. Scale bars in insets in (A-C) are 5 mm each.

Here $T(x,t)$ is the tension in the rod, and μ_s and $2\mu_s$ are the effective drag coefficients in the tangential and normal directions ($\mu_s \sim \mu$, up to logarithmic factors in the aspect ratio) obtained from slender body theory[17]. The accompanying boundary conditions are that at the free end $x=0$, $\partial_x^2 Y(0,t) = \partial_x^3 Y(0,t) = T(0,t) = 0$ while at the needle $x = L = vt$, the clamped boundary conditions read $Y(L,t) = \partial_x Y(L,t) = 0$.

Solving equation (4) to get $T = -\mu_s v x$ and substituting the result into Eq. (5) while using the ansatz $Y(x,t) = \eta(x)e^{\sigma t}$ to determine the growth rate of an instability σ yields the eigenvalue problem

$$2\mu_s\sigma\eta(x) + 2v\mu_s\eta'(x) + B\,\eta''''(x) + \mu_s v x \eta''(x) = 0. \tag{6}$$

Since $\eta \to -\eta$ is a symmetry of the equation for real solutions $\eta(x)$, the growth rate σ will also be real. At the onset of instability $\mathrm{Re}[\sigma] = \sigma = 0$ so that Eq. (6) can be rewritten in scaled form as

$$2\,\eta'(\xi) + \beta^{-1}\,\eta^{(4)}(\xi) + \xi\,\eta''(\xi) = 0, \tag{7}$$

where $x = L\xi$ and $\beta \equiv \mu_s v L^3/B$. By using the boundary conditions at the free end, the solution to this equation can be written as

$$\eta(\xi) = A + C\,\xi\;{}_0F_1\left(\frac{4}{3}; -\frac{\xi^3\beta}{9}\right), \tag{8}$$

where ${}_0F_1$ is the confluent hypergeometric function[18]. Using the boundary condition at the extruding end $\eta(1) = 0, \eta'(1) = 0$ then yields

$${}_0F_1\left(\frac{4}{3}; -\frac{\beta}{9}\right) = \frac{\beta}{4}\;{}_0F_1\left(\frac{7}{3}; -\frac{\beta}{9}\right), \tag{9}$$

a condition only satisfied for special values of β. Solving (9) numerically we find that this first happens for $\beta \approx 3.48$ and thus yields

$$\ell \approx 1.41\left(\frac{B}{\mu v}\right)^{1/3}. \tag{10}$$

The above equation also yields an expression for the oscillation frequency $\omega_c \equiv v/\ell \approx 0.71\,v^{4/3}(\mu/B)^{1/3}$. Numerical simulations of an elastic filament moving in a viscous fluid (described in Appendix A.3) with lengths just above and below the threshold given in Eq. 10 are consistent with this result, and provide a consistency check on the stability theory as well as simulation.

Using experimental parameter values in the range $B \sim Er^4$ (E =2.7 kPa, $r \sim$ 0.1-2 mm), $\mu \sim$0.001 Pa.s and $v \sim$2-70 mm/s, the experimentally obtained relation for the buckling length is $\ell \sim 1.04\,(B/\mu v)^{1/3}$ (Figs. 2A-B) while that for the frequency is $\omega \sim 1.1\,v^{4/3}\,(\mu/B)^{1/3}$ (Fig. 2C), in reasonable agreement with the values obtained from the formal calculation above.

Multiscale control of filament structure and morphology

We can use our understanding of the drag-induced coiling instability to control filament curvature. Since coiling is induced by ambient drag, if polymerization occurs slowly, filament curvature can get frozen in due to polymerization as a function of the scaled polymerization rate kd/v (here k is the polymerization rate, $v = Q_0/d^2$ is the flow velocity). At low flow rates, the tubes are relatively straight, while at higher flow rates, the tubes are strongly crumpled within an approximately conical plume (Fig.4A), with an opening angle θ that varies linearly with needle diameter(Fig.4B and Movie S3). In this strongly crumpled regime, the polymerized tubes have a disordered morphology driven by the coupled dynamics of flow and polymerization that occur on similar time scales. The morphology can be quantified in terms of the variance of the curvature of the center line of these tubes as a function of the flow rate Q_o (Fig.4C). Turning this bug into a feature suggests a method to fabricate filaments of varying curvature by controlling the needle diameter and the extrusion rate to 'freezes' the dynamic instability of the filament. Conversely, in this chaotic crumpling regime, the small scale roughness in the filaments (Appendix, Fig. A4) could also serve as a read out of the interfacial shear instability[19] between the vis-

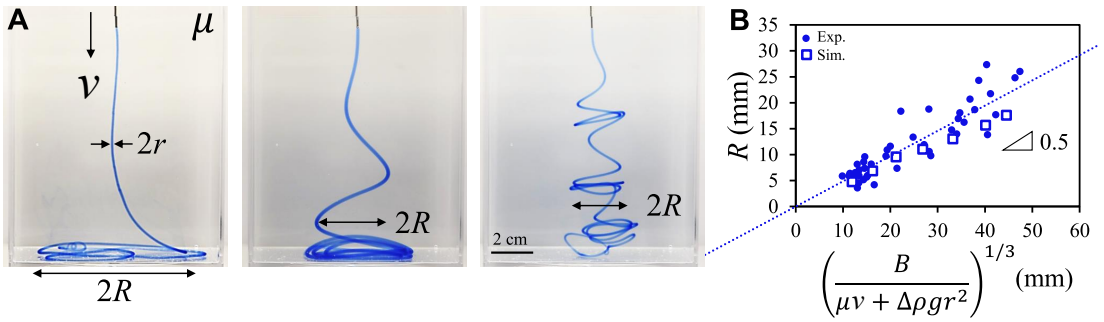

Fig. 3 Universal scaling to describe gravity induced rope coiling and drag-induced filament coiling during flow. (A) Pictures showing the gravity driven classical rope coiling (left: 18G needle, $d = 0.84$mm at Q_o=0.5ml/min), drag-induced elastic coiling (centre: 18G needle, $d = 0.84$mm at Q_o=5ml/min) and period doubling (right: 20G needle, $d = 0.6$mm at Q_o=5ml/min) (See Movie S2). (B) Universal scaling ($R \sim [B/(\mu v + \Delta\rho g r^2)]^{1/3}$) shows how the radius of coiling, R, of the polymerized alginate tubes collapses data ranging from the gravity driven classical rope coiling to the drag induced elastic tube coiling, with a slope of 0.5. The simulation data for the universal scaling fall close to the experimental data.

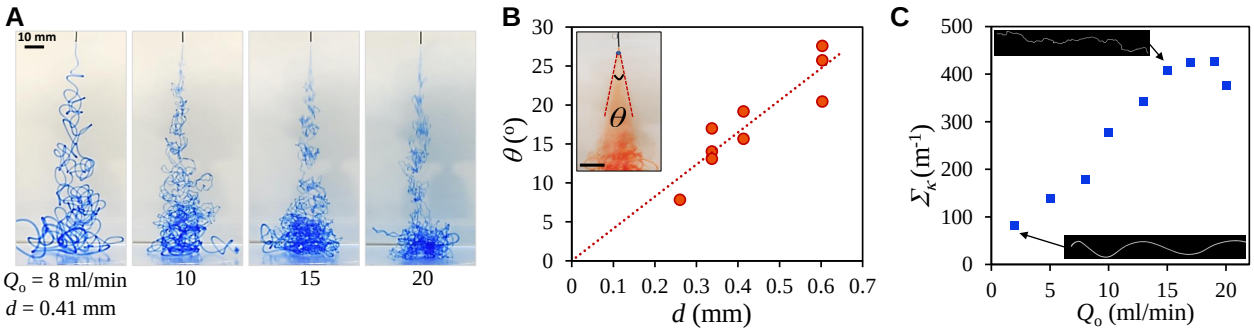

Fig. 4 Characterization of the chaotic plume. (A) Snapshots of the chaotic plume observed for high flow rates (Q_o) for a given needle (22G, d=0.41 mm) (See Movie S3). (B) The plume angle (θ) of the gel tubes in the chaotic regime formed at different inlet needle diameters (d) and extrusion rates (Q_o). θ increases linearly with needle diameter (d), and is weakly dependent on Q_o (depicted by the vertical spread at a given value of d and in A). Inset shows an example image of the plume shape, i.e, an averaged video of the experiment with 22G needle ($d = 0.41$mm) at Q_o=15 ml/min, where θ is measured from the point where the plume opens. Scale bar is 10 mm. (C) Characterization of the chaotic regime via standard deviation of curvature (Σ_κ) of the gel tubes formed at high extrusion rates for a specific needle (here 22G, $d = 0.41$mm). As Q_o increases, Σ_κ increases and then saturates at very high rates due to finite thickness of the tubes.

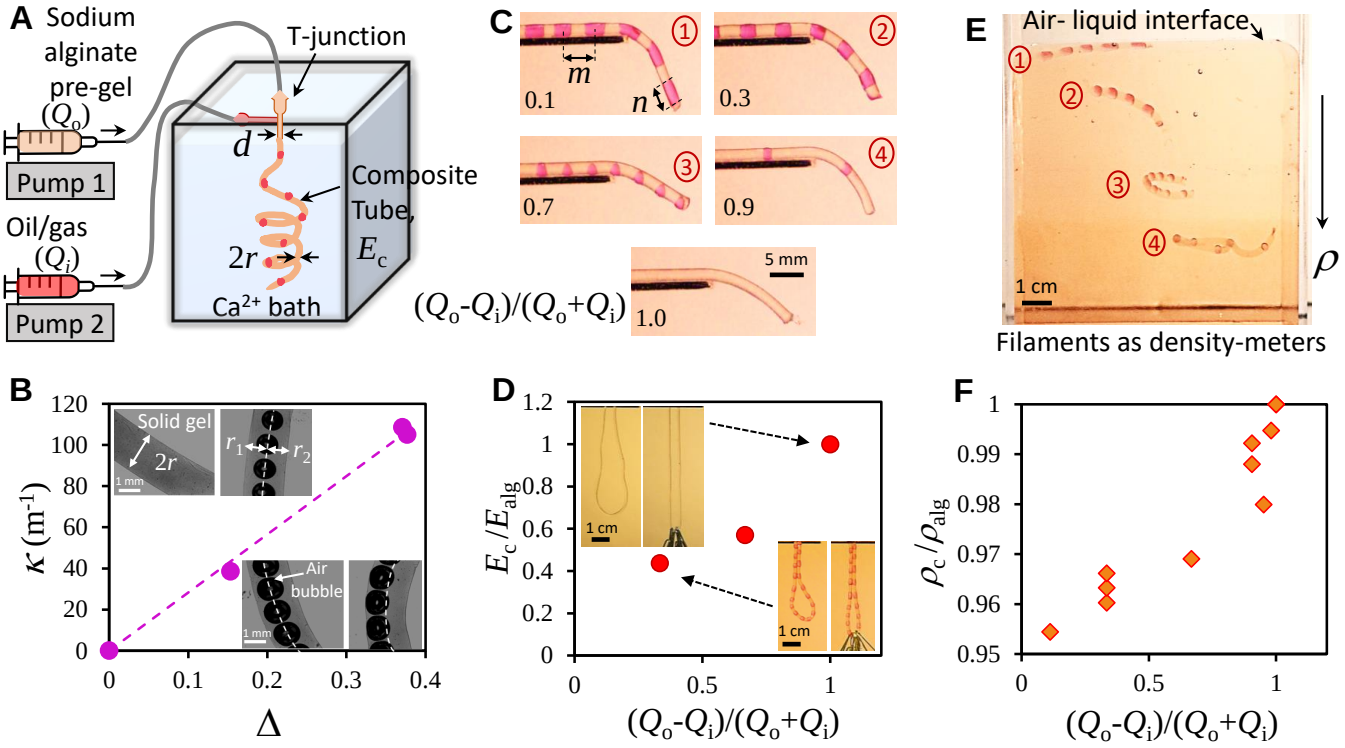

Fig. 5 Controlled patterning of co-extruded jelling jet. (A) Schematic of the experimental setup that is used to obtain composite fluid-in-solid tubes via polymerization of co-extruding two liquids (2% sodium alginate, Q_o and inner fluid, Q_i) into an aqueous bath containing 150 mM calcium chloride (needle inner diameter, d). A T-junction in the tubing allows the alginate solution and embedded fluid to meet, before entering the calcium bath. (B) Curvature can be controlled by the inclusion of air bubbles at a prescribed (mis)alignment with the central axis of the tube, quantified by $\Delta = (r_1 - r_2)/r$, which dictates composite tube curvature (κ). **(C-D) Controlling elastic moduli with inclusions:** (C) Gravity driven bending of small segments of composite filaments show that elastic moduli of filaments vary when oil droplets (silicone oil, kinematic viscosity ~100 cSt, $\rho_{oil} = 972 \text{kg/m}^3$, flow rate Q_i, dyed red) are co-extruded within the alginate (outer extrusion rate, Q_o). Varying the relative flow rates of oil and alginate $(Q_o - Q_i)/(Q_o + Q_i)$ controls filament morphology (spacing between oil inclusions, m and the size of the inclusions, n) and therefore elastic moduli. (D) The normalized elastic moduli of the composite tubes (E_c/E_{alg}) can be obtained by stretching the tubes (inset) and plotting the normalized ratio E_c/E_{alg} as a function of $(Q_o - Q_i)/(Q_o + Q_i)$. **(E-F) Controlling density with inclusions:** (E) The density of alginate tubes (pure, ρ_{alg}=1054 kg/m^3) can be lowered by introducing oil inclusions ($\rho_{oil} = 972$ kg/m^3) to form composite tubes (ρ_c, 1: 1006 kg/m^3; 2: 1018 kg/m^3; 3: 1021 kg/m^3; 4: 1045 kg/m^3). Suspending these filaments in a density gradient column serve as a direct readout for the density (ρ_c) of the column as the filaments become neutrally buoyant at a height where their density is equal to the density of the liquid at that height. Here, the density at the bottom of the container is 1050 kg/m^3 and at the air liquid interface is 1010 kg/m^3. (F) The normalized density of the composite tubes (ρ_c/ρ_{alg}) are plotted as a function of $(Q_o - Q_i)/(Q_o + Q_i)$.

coelastic sodium alginate jet and the Newtonian fluid aqueous calcium chloride bath.

In addition to controlling the global morphology of the filament, we can also control its local structure and properties such as its buoyancy, rigidity, and curvature. To do so, we introduce a second fluid such as an oil (e.g. silicone oil, $\rho_{oil} \sim 972$ kg/m^3), or a gas (e.g. compressed nitrogen) that is internally co-extruded with the alginate solution, as shown schematically in Fig. 5A (Movie S5). At low co-extrusion rates, the internal fluid pinches off due to interfacial forces, and forms small droplet inclusions. By varying the relative flow rates of the co-extruding fluid (Q_i) and the encasing alginate (Q_o), we can control the size, spacing and position of the fluid droplet inclusions in the gel filaments. By (mis)aligning the gas bubbles relative to the axis of the filament (Fig. 5B), we can control filament curvature. By varying the fraction of internal droplets of oil or gas, we can also control the effective filament bending and stretching stiffness (Figs. 5 C-D and Appendix, A3 C-D) as well as the filament density and buoyancy (Figs. 5 E-F). All together, this allows us then to print and write out stable structures in the ambient liquid by dynamically varying the co-extrusion rate of the internal fluid (oil/gas) and the extrusion of the alginate, as seen in Fig. 5.

Conclusions

Complementing the study of fluid filament coiling driven by boundary compression seen in the familiar honey-on-toast experiment, here we have examined the coiling of a submerged jelling jet driven by bulk drag. A combination of experimental observations, scaling analysis, stability theory and simulations allowed us to characterize the onset and the nonlinear evolution of periodic coiling. We then explored the possibility of controlling this instability to create complex structures. By harnessing the simplest instabilities in elastic filaments and fluid jets, namely the buckling of a slender elastic filament and the breakup of a slender liquid jet, we showed how to create a quasi-one dimensional liquid-solid composite. The co-extrusion a thin stream of aqueous

sodium alginate and a second liquid into a reacting calcium chloride bath leads to the the pinch off of the internal liquid to form a beaded filament that buckles and coils. By controlling the relative rates of polymerization of the sodium alginate, with calcium ions concentration, and the mechanical instability of the freshly formed filaments, we demonstrated the use the underlying dynamical processes to write in three dimensions while controlling filament properties such as buoyancy, stiffness, curvature as well as chirality. Our ability to control and steer the shape of the soft filaments using an instability stands in sharp contrast with the deterministic approach used to deposit each voxel in the additive manufacturing process[20] and suggests alternative ways to manufacture and engineer low-dimensional fluid-solid composites[21–23] for various applications[24,25].

Acknowledgements

For partial financial support, we thank the National Science Foundation grants NSF DMR 20-11754, NSF DMREF 19-22321, and NSF EFRI 18-30901.

Conflicts of interest

There are no conflicts to declare.

References

1 L. Mahadevan and J. B. Keller, *Proceedings of the Royal Society of London. Series A: Mathematical, Physical and Engineering Sciences*, 1996, **452**, 1679–1694.

2 M. Habibi, N. Ribe and D. Bonn, *Physical Review Letters*, 2007, **99**, 154302.

3 M. K. Jawed, F. Da, J. Joo, E. Grinspun and P. M. Reis, *Proceedings of the National Academy of Sciences*, 2014, **111**, 14663–14668.

4 G. I. Taylor, *Proc. Intl. Congress on Theor. Appl. Mechanics*, Springer, 1969, pp. 382–388.

5 L. Mahadevan, W. S. Ryu and A. D. Samuel, *Nature*, 1998, **392**, 140.

6 L. Mahadevan, W. Ryu and A. Samuel, *Nature*, 2000, **403**, 1038.

7 N. M. Ribe, *Journal of Fluid Mechanics*, 2017, **812**, R2.

8 H.-Y. Kim, M. Lee, K. J. Park, S. Kim and L. Mahadevan, *Nano letters*, 2010, **10**, 2138–2140.

9 P.-T. Brun, C. Inamura, D. Lizardo, G. Franchin, M. Stern, P. Houk and N. Oxman, *Philosophical Transactions of the Royal Society A: Mathematical, Physical and Engineering Sciences*, 2017, **375**, 20160156.

10 C. Hu, M. Nakajima, H. Wang, T. Yue, Y. Shen, M. Takeuchi, Q. Huang, M. Seki and T. Fukuda, 2013 13th IEEE International Conference on Nanotechnology (IEEE-NANO 2013), 2013, pp. 529–534.

11 P. Dilworth and M. Bogue, *Hand-held three-dimensional drawing device*, 2015, US Patent 9,102,098.

12 Y.-M. Lin and G. C. Rutledge, *Journal of membrane science*, 2018, **563**, 247–258.

13 P. Lee and M. Rogers, *International Journal of Gastronomy and Food Science*, 2012, **1**, 96–100.

14 K. Machin, *Journal of Experimental Biology*, 1958, **35**, 796–806.

15 F. Gosselin, P. Neetzow and M. Paak, *Physical Review E*, 2014, **90**, 052718.

16 L. Mahadevan and J. B. Keller, *Siam Review*, 1999, **41**, 115–131.

17 R. G. Cox, *Journal of Fluid Mechanics*, 1970, **44**, 791–810.

18 G. E. Andrews, R. Askey and R. Roy, *Special functions*, Cambridge university press, 1999, vol. 71.

19 S. Yamani, B. Keshavarz, Y. Raj, T. A. Zaki, G. H. McKinley and I. Bischofberger, *Physical Review Letters*, 2021, **127**, 074501.

20 M. A. Skylar-Scott, J. Mueller, C. W. Visser and J. A. Lewis, *Nature*, 2019, **575**, 330–335.

21 R. W. Style, R. Tutika, J. Y. Kim and M. D. Bartlett, *Advanced Functional Materials*, 2021, **31**, 2005804.

22 M. D. Bartlett and R. W. Style, *Soft Matter*, 2020, **16**, 5799–5800.

23 L. Cai, J. Marthelot and P.-T. Brun, *Proceedings of the National Academy of Sciences*, 2019, **116**, 22966–22971.

24 H. Onoe, T. Okitsu, A. Itou, M. Kato-Negishi, R. Gojo, D. Kiriya, K. Sato, S. Miura, S. Iwanaga, K. Kuribayashi-Shigetomi *et al.*, *Nature materials*, 2013, **12**, 584–590.

25 L. Hu, M. Pasta, F. La Mantia, L. Cui, S. Jeong, H. D. Deshazer, J. W. Choi, S. M. Han and Y. Cui, *Nano letters*, 2010, **10**, 708–714.

26 R. Kolluri, *ACM Transactions on Algorithms (TALG)*, 2008, **4**, 1–25.

27 A. Nealen, *URL: http://www. nealen. com/projects*, 2004, **130**, 25.

28 M. Bergou, M. Wardetzky, S. Robinson, B. Audoly and E. Grinspun, *ACM SIGGRAPH 2008 papers*, 2008, pp. 1–12.

29 R. Goldenthal, D. Harmon, R. Fattal, M. Bercovier and E. Grinspun, *ACM SIGGRAPH 2007 papers*, 2007, pp. 49–es.

30 L. Mahadevan, W. S. Ryu and A. D. Samuel, *Nature*, 1998, **392**, 140–140.

31 M. K. Jawed, F. Da, J. Joo, E. Grinspun and P. M. Reis, *Proceedings of the National Academy of Sciences*, 2014, **111**, 14663–14668.